

The Origin of Nematic Order in the Iron-Based Superconductors

S. Avci*,¹ O. Chmaissem,^{1,2} S. Rosenkranz,¹ J. M. Allred,¹ I. Eremin,³ A. V. Chubukov,⁴ D. Y. Chung,¹ M. G. Kanatzidis,^{1,5} J.-P. Castellán,¹ J. A. Schlueter,¹ H. Claus,¹ D. D. Khalyavin,⁶ P. Manuel,⁶ A. Daoud-Aladine,⁶ and R. Osborn¹

¹*Materials Science Division, Argonne National Laboratory, Argonne, IL 60439-4845, USA*

²*Physics Department, Northern Illinois University, DeKalb, IL 60115, USA*

³*Ruhr-Universität Bochum, Theoretische Physik III, 44801 Bochum, Germany*

⁴*Department of Physics, University of Wisconsin-Madison, Madison, Wisconsin 53706, USA*

⁵*Department of Chemistry, Northwestern University, Evanston, IL 60208-3113, USA*

⁶*ISIS Pulsed Neutron and Muon Facility, Rutherford Appleton Laboratory, Chilton, Didcot OX11 0QX, United Kingdom*

(Dated: March 13, 2013)

A theory of superconductivity in the iron-based materials requires an understanding of the phase diagram of the normal state. In these compounds, superconductivity emerges when stripe spin density wave (SDW) order is suppressed by doping, pressure or disorder, suggesting a possible role for magnetic fluctuations in the pairing mechanism. Experimentally, SDW order is often pre-empted by nematic order whose phase transition occurs at a slightly higher temperature but whose origin is yet to be resolved. One scenario is that the nematic order is unrelated to magnetism and reflects an orbital ordering of the iron 3d-electrons. This ordering triggers the anisotropic magnetic coupling that produces stripe SDW order at a lower T . Another scenario is that stripe-SDW magnetism is the primary instability, but the magnetic transition occurs in two steps: first four-fold spin-rotational symmetry gets broken and the system develops spin-nematic order, and then time-reversal symmetry also gets broken, and full stripe-SDW order develops. Because spin-nematic order also induces orbital order, it is difficult to distinguish between the two scenarios experimentally. In this letter, we show that the magnetic scenario predicts that, at high doping, the system should undergo a transition at $T < T_N$ into a new SDW phase in which four-fold rotational symmetry is restored. We have now observed a first-order transition to such a phase in $\text{Ba}_{0.76}\text{Na}_{0.24}\text{Fe}_2\text{As}_2$, in good agreement with the spin-nematic model.

INTRODUCTION

There have been extensive investigations of the phase diagrams of the various iron arsenide and chalcogenide structures that display high temperature superconductivity with critical temperatures up to 55 K [1–4]. In common with other unconventional superconductors, such as the copper oxides, heavy fermions, and organic charge-transfer salts, superconductivity is induced by suppressing a magnetically ordered phase, which generates a high density of magnetic fluctuations that could theoretically bind the Cooper pairs. Whether this is responsible for the high transition temperatures has not been conclusively established, but it makes the origin of the magnetic interactions an important issue to be resolved [5, 6].

In nearly all the iron arsenides and chalcogenides, the iron atoms form a square planar net and the magnetic order consists of ferromagnetic stripes along one iron-iron bond direction that are antiferromagnetically aligned along the orthogonal iron-iron bond [6, 7]. These systems are metallic and the Fermi surfaces, which are formed by the iron 3d electrons, are nearly cylindrical with hole pockets at the centre of the Brillouin zone and

electron pockets at the zone boundaries, all of similar size. In such an electronic structure, interactions between electrons near the hole and electron pockets give rise to a spin density wave (SDW) order at the wavevector connecting the two pockets [8]. This itinerant picture is consistent with the wavevector of the observed antiferromagnetism, Angle Resolved Photoemission (ARPES) measurements of the electronic structure [9, 10], and the evolution of the dynamic magnetic susceptibility with carrier concentration [11–13].

However, any theory of the magnetic order also has to explain the structural transition which occurs at a temperature either just above or coincident with the SDW transition and lowers the symmetry from tetragonal (C_4) to orthorhombic (C_2). This is often referred to as nematic order, and the relation between nematicity, magnetic order, and superconductivity has become one of the central questions in the iron-based superconductors [14, 15].

At present, there are two scenarios for the development of the nematic order and its relation to SDW order. In the first, the structural order is unrelated to magnetism and is driven by orbital ordering as the primary instability. The orbital ordering induces magnetic anisotropy and triggers the magnetic transition at a lower temperature by renormalizing the exchange constants [16–18]. This scenario is largely phenomenological, but there have been recent efforts to put it into a microscopic basis [19].

In the second scenario, the structural order is driven

*Current address: Department of Metallurgical and Materials Engineering, Bursa Technical University, 16190 Bursa, Turkey

by magnetic fluctuations, associated with the fact that striped SDW order can be along the x -axis (ordered momentum is $\mathbf{Q}_X = (0, \pi)$) or along the y -axis (ordered momentum is $\mathbf{Q}_Y = (\pi, 0)$). Theory predicts that the Z_2 symmetry between the X and Y directions can be broken above the true SDW ordering temperature that breaks $O(3)$ spin symmetry, *i.e.*, the system distinguishes between \mathbf{Q}_X and \mathbf{Q}_Y without breaking time-reversal symmetry [20]. The order parameter of this “Ising-spin-nematic state” couples linearly to the lattice, inducing both structural and orbital order. The magnetic scenario has been developed for itinerant [8, 20] and localized [21–24] fermions, and the phase diagrams are rather similar in the two approaches. Below we use the fact that the systems we study are metals and use an itinerant approach.

It is difficult to distinguish the orbital and the magnetic scenarios since many of the observable properties are identical. We have now identified both theoretically and experimentally a new magnetic phase that can distinguish the two scenarios. By extending our previous analysis of the itinerant model to higher carrier concentrations, we have discovered that the phase diagram is richer than previously anticipated, based on the Ginzburg-Landau analysis near T_N , and that there exists, in some range of parameters, an additional phase at $T < T_N$, that restores C_4 symmetry. The order parameter in this new phase combines \mathbf{Q}_X and \mathbf{Q}_Y with equal weights. In the following, we summarize the results of these calculations, which are explained in more detail in the Supplementary Information, and show experimental evidence for the predicted phase in a hole-doped superconductor, $\text{Ba}_{0.76}\text{Na}_{0.24}\text{Fe}_2\text{As}_2$. Such a second transition is highly unlikely in the orbital scenario because the breaking of the symmetry between \mathbf{Q}_X and \mathbf{Q}_Y is the pre-condition for a magnetic transition. We view the observation of the transition to an SDW state which does not break the symmetry between \mathbf{Q}_X and \mathbf{Q}_Y as a strong indication that the nematic order is of magnetic origin rather than of orbital origin.

THEORY

The itinerant description of magnetism in iron-based superconductors is built upon the fact that the hole bands are centered around $\mathbf{Q}_\Gamma = (0, 0)$ and the electron bands are centered at $\mathbf{Q}_X = (\pi, 0)$ and $\mathbf{Q}_Y = (0, \pi)$, respectively (Fig. 1(a)). A spin susceptibility is logarithmically enhanced at momenta connecting hole and electron pockets, and SDW order develops even if the interaction is weak. The SDW order parameter is in general a combination of the two vector components Δ_X and Δ_Y with momenta $(\pi, 0)$ and $(0, \pi)$, respectively. For a model of perfect Fermi surface nesting (circular hole and electron pockets of equal radii) and only electron-hole inter-

actions, SDW order specifies $|\Delta_X|^2 + |\Delta_Y|^2$ but not the relative magnitudes and directions of Δ_X and Δ_Y . Away from perfect nesting, the ellipticity of the electron pockets and interactions between the electron bands break the degeneracy and lower the symmetry of the SDW order. Near T_N , an analysis within a Ginzburg-Landau expansion in powers of Δ_X and Δ_Y shows that fourth-order terms select stripe magnetic order with either $\Delta_X \neq 0$, $\Delta_Y = 0$, or $\Delta_Y \neq 0$, $\Delta_X = 0$ [8, 20]. Such an order simultaneously reduces the lattice C_4 symmetry down to C_2 . The order parameter in the stripe phase is shown schematically in Fig.1(b).

An issue that has not been discussed in detail until now is whether another magnetic ground state, in which both Δ_X and Δ_Y are non-zero, may appear at a lower temperature, as a result of non-linear effects. This might happen either via a first-order transition, in which case the most likely outcome is the state in which $|\Delta_X| = |\Delta_Y|$ (see Fig.1(c)), or via a second-order transition, in which case the second order parameter appears continuously and likely remains relatively small down to $T = 0$ (see Fig.1(d)).

To check for a potential second SDW transition, we extended the previous Ginzburg-Landau analysis to the entire temperature range by solving non-linear coupled mean-field equations for Δ_X and Δ_Y and analyzing which solution minimizes the free energy. This has revealed new features in the phase diagram not previously identified. In particular, we find that SDW order with $\Delta_X = \Delta_Y$, which breaks $O(3)$ spin symmetry but preserves lattice C_4 symmetry, does emerge at low T , as the mismatch in hole and electron pocket sizes grows.

We obtained this result by analyzing the minimal three-band model with one hole and two electron pockets. For simplicity, we considered parabolic dispersions with

$$\xi_{\Gamma, \mathbf{k}} = \varepsilon_0 - \frac{k^2}{2m} - \mu \quad (1)$$

$$\xi_{X, \mathbf{k}+\mathbf{Q}_X} = -\varepsilon_0 + \frac{k_x^2}{2m_x} + \frac{k_y^2}{2m_y} - \mu \quad (2)$$

$$\xi_{Y, \mathbf{k}+\mathbf{Q}_Y} = -\varepsilon_0 + \frac{k_x^2}{2m_x} + \frac{k_y^2}{2m_y} - \mu \quad (3)$$

where m_i are band masses, ε_0 is the offset energy, and μ is the chemical potential.

The non-interacting Hamiltonian takes the form

$$\mathcal{H}_0 = \sum_{i, \mathbf{k}} \xi_{i, \mathbf{k}} c_{i, \mathbf{k}\alpha}^\dagger c_{i, \mathbf{k}\alpha} \quad (4)$$

where $i = 1 - 3$ label the bands, the summation over repeated spin indices α is assumed, and we shift the momenta of the fermions near the X and Y Fermi pockets by \mathbf{Q}_X and \mathbf{Q}_Y , respectively, writing $\xi_{X, \mathbf{k}+\mathbf{Q}_X} = \xi_{2, \mathbf{k}}$, $\xi_{Y, \mathbf{k}+\mathbf{Q}_Y} = \xi_{3, \mathbf{k}}$.

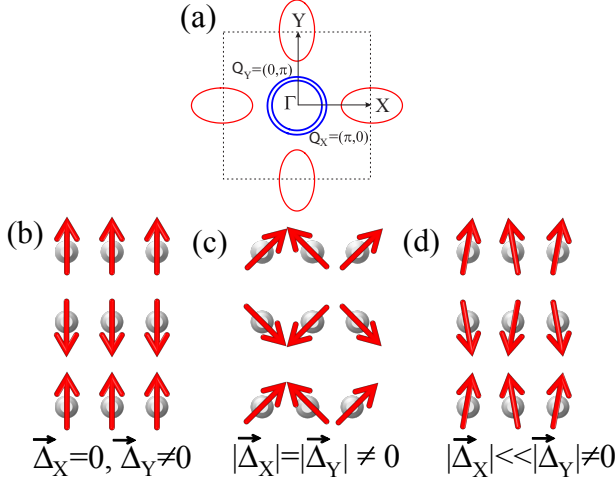


FIG. 1: (a) (upper panel) The band-structure with two circular hole pockets at Γ and two electron pockets at X and Y, using the unfolded Brillouin zone with one Fe atom per unit cell. The arrows refer to two equivalent nesting wavevectors $\mathbf{Q}_X = (\pi, 0)$ and $\mathbf{Q}_Y = (0, \pi)$ (lower panel) Possible magnetic ground states of the Fe-lattice: (b) the C_2 antiferromagnetic stripe phase with $\Delta_X = 0$ and $\Delta_Y \neq 0$; (c) a C_4 magnetic state, in which $|\Delta_X| = |\Delta_Y| \neq 0$, that is compatible with tetragonal lattice symmetry (other possible C_4 magnetic structures are discussed in the Supplementary Information); (d) magnetic order in which $|\Delta_X| \ll |\Delta_Y| \neq 0$. Note that the Néel transition at low temperatures, T_{N_2} , from phase (b) to phase (c) is first order, while the transition from phase (b) to phase (d) is of the second order in which an additional small component of Δ_X appears below T_{N_2} . Our experiments are more compatible with scenario (c).

The interaction term in the Hamiltonian \mathcal{H}_{int} contains all symmetry-allowed interactions between low-energy fermions, which include inter- and intra-band scattering processes [25]. We present the explicit form of \mathcal{H}_{int} in the Supplementary Information. The mean-field equations on Δ_X and Δ_Y are obtained by introducing $\Delta_X = (1/2N) \sum_{\mathbf{k}} c_{1,\mathbf{k}\alpha}^\dagger \tilde{\sigma}_{\alpha\beta} c_{2,\mathbf{k}\beta}$ and $\Delta_Y = (1/2N) \sum_{\mathbf{k}} c_{1,\mathbf{k}\alpha}^\dagger \tilde{\sigma}_{\alpha\beta} c_{3,\mathbf{k}\beta}$ and using them to decouple four-fermion terms into anomalous quadratic terms with inter-band "hopping", which depends on Δ_X and Δ_Y . We diagonalized the quadratic form, re-expressed $c_{i,\mathbf{k}\alpha}$ in terms of new operators and obtained a set of two coupled self-consistent equations for Δ_X and Δ_Y .

We solved the mean-field equations numerically as a function of two parameters, δ_0 and δ_2 (see Supplementary Information for details). The parameter $\delta_0 = 2\mu$ represents the mismatch in chemical potentials of the hole and electron pockets ($\delta_0 = 0$ when the electron and hole pockets are identical). $\delta_2 = \varepsilon_0 m(m_x - m_y)/(2m_x m_y)$ is proportional to the ellipticity of the electron pockets. We focused on the two SDW-ordered states— the antiferromagnetic stripe state with $\Delta_X \neq 0$ and $\Delta_Y = 0$, in which C_4 -symmetry is reduced to C_2 and on the SDW state with $\Delta_X = \Delta_Y$, in which C_4 -symmetry is pre-

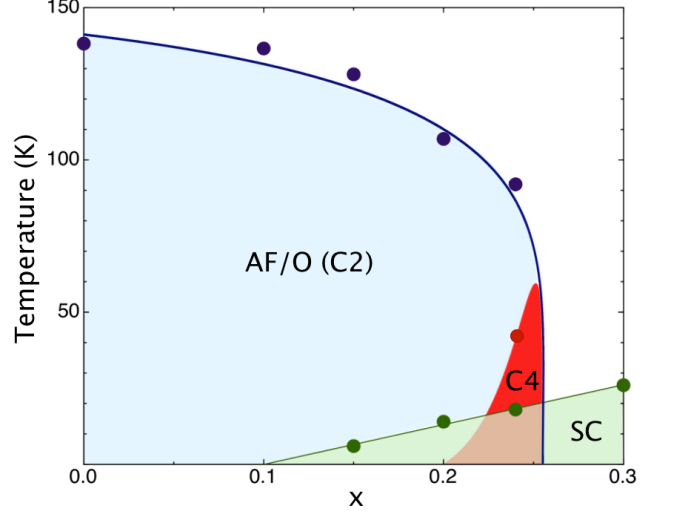


FIG. 2: Phase diagram of $\text{Ba}_{1-x}\text{Na}_x\text{Fe}_2\text{As}_2$. The blue points are the coincident antiferromagnetic and orthorhombic transition temperatures, T_N , into the C_2 phase, and the red point is the observed transition temperature into the tetragonal C_4 phase, all measured by neutron diffraction. The green points are the superconducting transition temperatures, T_c , determined from magnetization data.

served. As we said, the two states are degenerate at zero ellipticity and perfect nesting, when $\delta_2 = \delta_0 = 0$. Once the ellipticity becomes non-zero, the stripe state wins immediately below the Neel temperature T_N . The C_4 -preserving state (with $\Delta_X = \Delta_Y$) is a local maximum and is unstable at $T \leq T_N$.

By solving the equations at lower temperature, we found that, at a finite δ_0 , the C_4 -preserving state also becomes locally stable below some $T < T_N$, and at an even lower $T < T_{N_2}$, its free energy becomes smaller than that of the stripe phase, *i.e.*, at $T = T_{N_2}$ the system undergoes a first-order phase transition in which lattice C_4 symmetry gets restored. (see Fig.1(c)). Because T_N falls as the Fermi surface mismatch δ_0 increases, the new C_4 -preserving phase in practice exists only in a narrow region of the phase diagram close to the suppression of SDW order. This behavior is illustrated in Fig. 2. We also analyzed a four-pocket model with two hole pockets and found another scenario for a second SDW transition. Namely, the AF stripe order Δ_Y initially involves only fermions from a hole pocket which has higher density of states. Below some $T < T_N$, fermions near the remaining hole pocket and near the electron pocket at X, not involved in the initial stripe order, also produce SDW instability, and the system gradually develops the second order parameter $|\Delta_X|$, which distorts the stripe AF order. The corresponding low T spin configuration is shown in Fig.1(d). In this case, however, the C_4 symmetry remains broken at all temperatures. Our experimental data taken as a function of doping are more consistent with a first-order transition and restoration of C_4 symmetry (see

below). It is possible, however, that the second scenario is realized under pressure [26].

EXPERIMENT

We are currently exploring the phase diagram of $\text{Ba}_{1-x}\text{Na}_x\text{Fe}_2\text{As}_2$ using neutron and x-ray powder diffraction, following our recent investigation of the potassium-doped compounds [1]. Details of the synthesis and characterization of the polycrystalline samples and the powder diffraction measurements are given in the Methods section below. In both series, the addition of the alkali metal dopes holes into iron d -bands, which is equivalent to reducing the chemical potential, μ , in the model described above. This has the effect of reducing the transition temperature into the stripe phase from 139 K, in the parent compound BaFe_2As_2 , to 0 at $x \sim 0.25$ in both the K-doped and Na-doped series. One unusual feature of both series is that the antiferromagnetic and orthorhombic transitions are coincident and first-order over the entire phase diagram [28], an observation that is quite unambiguous since both order parameters are determined from the same neutron powder diffraction measurement.

We will publish a more detailed report on the whole phase diagram of $\text{Ba}_{1-x}\text{Na}_x\text{Fe}_2\text{As}_2$ in a forthcoming publication, but to understand its significance to this article, we show in Fig. 2 the transition temperatures into the antiferromagnetic/orthorhombic (AF/O) C_2 (T_N) and superconducting phases (T_c) up to $x = 0.3$. In $\text{Ba}_{1-x}\text{K}_x\text{Fe}_2\text{As}_2$, it was possible to fit T_N vs x to a scaling form, *i.e.*, to $(1 - x/x_c)^{2\beta}$, with $x_c = 0.252$ and $\beta = 0.125$ [1]. We do not have as many data points in the sodium-doped system, but the phase diagram is extremely similar so we have assumed that the same scaling curve applies here as well. This scaling has not been observed in the other iron-based superconductors and may reflect the reduced disorder in these hole-doped compounds, in which the doping occurs away from the iron arsenide layers.

The only member of the sodium series to show a significant departure from the potassium compounds is at $x = 0.24$ close to the suppression of the AF/O order, which has a superconducting transition temperature of 24 K. The transition into the conventional C_2 phase occurs at 90 K. However, at $T_{N_2} = 39$ K, there is a remarkable first-order phase transition, at which the sample phase separates into regions with two different atomic and magnetic structures. Fig. 3(a) shows the orthorhombic splitting of the (112) nuclear Bragg peak at 90 K and its recombination at T_{N_2} marking the onset of a reentrant tetragonal phase. Not all the sample transforms back to C_4 symmetry. From a multi-phase Rietveld refinement, we estimate that approximately 40% of the sample remains in the orthorhombic phase below the transition (Fig. 4(a)). It is nevertheless clear that the whole sample

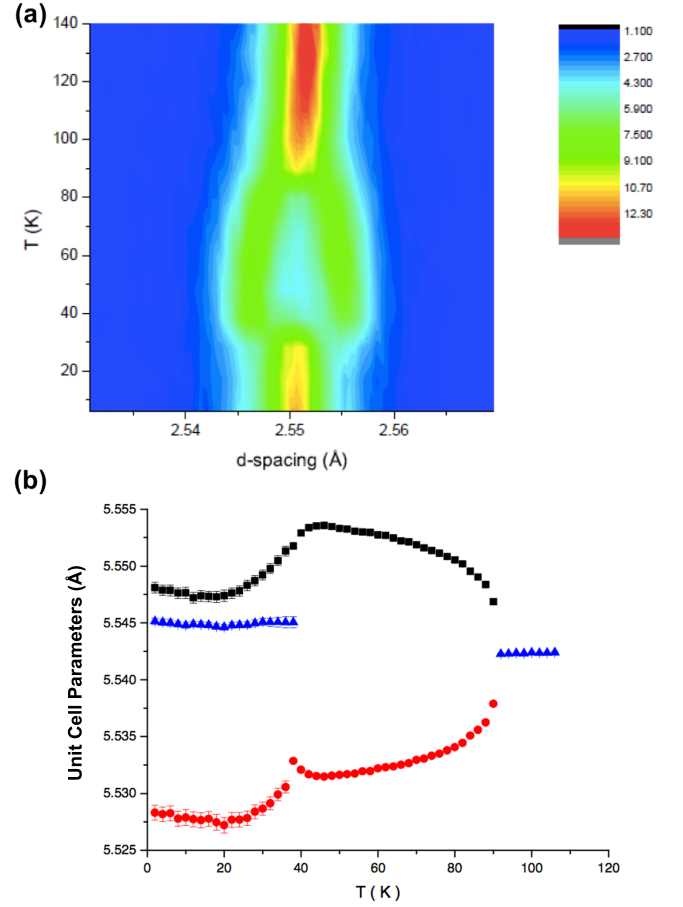


FIG. 3: First-order phase transition in $\text{Ba}_{0.76}\text{Na}_{0.24}\text{Fe}_2\text{As}_2$. (a) A neutron diffractogram from the Wish Diffractometer showing the orthorhombic splitting of the (112) Bragg peak at $T_N = 89$ K and its recombination at the reentrant tetragonal phase at 38 K. (b) The lattice parameters, a (blue points) in the tetragonal phase of $I4/mmm$ symmetry above T_N and below the reentrant transition, and a (red points) and b (black points) in the orthorhombic phase of $Fmmm$ symmetry below T_N . The tetragonal lattice parameter is multiplied by $\sqrt{2}$.

is involved in the first-order transition even if only a fraction is transformed because, even within the orthorhombic phase, the in-plane lattice parameters relax below the transition (Fig. 3(b)). The in-plane lattice parameters show a reduction in the low-temperature C_2 phase with an increase in the c -axis lattice parameter, *i.e.*, the high- and low-temperature C_2 phases are not identical. The C_4 phase shows the opposite trend, which means that the in-plane lattice parameter is slightly higher than above T_N . The overall volume is roughly constant through the reentrant transition for both phases.

Both the high-temperature and low-temperature C_2 phases have identical magnetic order with the moment in the plane, equivalent to the conventional AF stripe phase observed at other compositions. Within the high-temperature phase, the temperature dependence of the magnetic and orthorhombic order parameters are directly

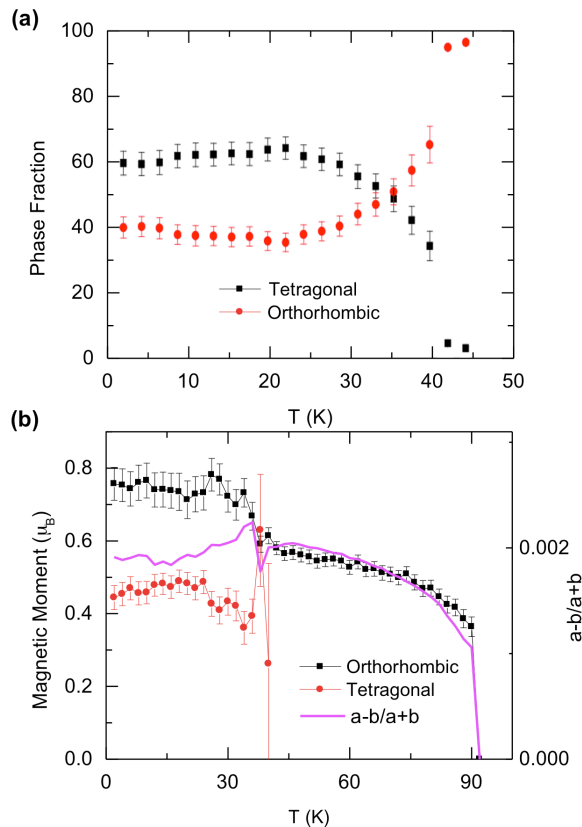


FIG. 4: (a) The temperature dependence of the phase fractions of the tetragonal C_4 phase (red points) and the orthorhombic C_2 phase (black points) below the reentrant transition at 40 K derived from two phase Rietveld refinements. (b) The temperature dependence of the magnetic moment in the tetragonal C_4 phase (red points), and the magnetic moment (black points) and orthorhombic order parameter $\delta = (a - b)/(a + b)$ (gold points) in the orthorhombic C_2 phase both above and below the reentrant phase transition.

proportional (Fig. 4(b)), as we saw in the K-doped series [28]. There is some evidence of phase competition above the reentrant transition since the moment in the low-temperature orthorhombic phase increases abruptly at the transition. The C_4 phase is also magnetically ordered. An unambiguous refinement of the magnetic structure will require measurements on single crystals, but possible solutions that are consistent with the structural space group ($I4/mmm$) and the lack of any in-plane magnetoelastic distortion are discussed in the Supplementary Information. They include the in-plane magnetic order illustrated in Fig. 1(c), as well as variants, in which the moments are aligned along the c -axis. Since the theory does not include spin-orbit coupling, both solutions are theoretically allowed.

DISCUSSION

It is important to distinguish these new results from previous observations of a reentrant tetragonal phase in electron-doped compounds, such as $\text{BaFe}_{2-x}\text{Co}_x\text{As}_2$ [29]. All those transitions were within the superconducting phase and have been convincingly shown to result from the competition between superconductivity and antiferromagnetic stripe order [30, 31]. The reentrant phase that we report here occurs well above the superconducting transition temperature and so requires a different explanation. We are also unaware of any model of orbital order that would predict a reentrant non-orbitally-ordered phase at lower temperature. Our results are broadly consistent with the itinerant model described above and are a natural consequence of magnetic order induced by the interaction between the hole and electron pockets suggested by the Fermi surface geometry.

The relaxation of the lattice parameters below the reentrant transition implies that there is some phase competition between the C_2 and C_4 phases in the high-temperature phase that is relieved below T_{N_2} . In principle, this could be modeled theoretically by extending the mean-field theory calculations performed so far to the more microscopic theory. Such a theory would be necessary to study a C_2 phase above the reentrant transition in which $\Delta_x \neq \Delta_y$ but both are non-zero. Nevertheless, the prediction that a C_4 phase can become degenerate with the C_2 phase only at higher doping when the hole and electron Fermi surfaces are not as well-matched in size, and that the stability of the C_4 phase would be limited to a very narrow region close to the suppression of antiferromagnetism is borne out by the new data.

Our results provide strong evidence for the validity of an itinerant model of nematic order in the iron-based superconductors, in which the orbital reconstruction of the iron $3d$ states is a consequence of magnetic interactions induced by Fermi surface nesting. Whether nematic order, or at least strong nematic fluctuations, is a prerequisite for superconductivity is another challenge to address in the future.

ACKNOWLEDGEMENTS

We are thankful to J. Knolle, R. Fernandes, J. Schmalian, R. Moessner, and V. Stanev for useful discussions. This work was supported by the Materials Sciences and Engineering Division of the Office of Basic Energy Sciences, Office of Science, U.S. Department of Energy, under contract #DE-AC02-06CH11357 (S.A., O.C., S. R., J.A., D.Y.C., M.G.K., J.-P.C., J.A.S., H.C., R.O.) and grant #DE-FG02-ER46900 (A.V.C.). I.E. acknowledges financial support from the German Academic Exchange Service (DAAD PPP USA Grant No. 50750339).

-
- [1] Stewart, G. Superconductivity in iron compounds. *Rev. Mod. Phys.* **83**, 1589–1652 (2011).
- [2] Paglione, J. & Greene, R. L. High-temperature superconductivity in iron-based materials. *Nature Phys.* **6**, 645–658 (2010).
- [3] Johnston, D. C. The puzzle of high temperature superconductivity in layered iron pnictides and chalcogenides. *Adv. Phys.* **59**, 803–1061 (2010).
- [4] Canfield, P. C. & Bud'ko, S. FeAs-Based Superconductivity: A Case Study of the Effects of Transition Metal Doping on BaFe_2As_2 . *Ann. Rev. Cond. Matt. Phys.* **1**, 27–50 (2010).
- [5] Dai, P., Hu, J. & Dagotto, E. Magnetism and its microscopic origin in iron-based high-temperature superconductors. *Nature Phys.* **8**, 709–718 (2012).
- [6] Lumsden, M. D. & Christianson, A. D. Magnetism in Fe-based superconductors. *J. Phys. Cond. Matt.* **22**, 203203 (2010).
- [7] de la Cruz, C. *et al.* Magnetic order close to superconductivity in the iron-based layered $\text{LaO}_{1-x}\text{F}_x\text{FeAs}$ systems. *Nature* **453**, 899–902 (2008).
- [8] Eremin, I. & Chubukov, A. V. Magnetic degeneracy and hidden metallicity of the spin-density-wave state in ferropnictides. *Phys. Rev. B* **81**, 024511 (2010).
- [9] Ding, H. *et al.* Observation of Fermi-surface-dependent nodeless superconducting gaps in $\text{Ba}_{0.6}\text{K}_{0.4}\text{Fe}_2\text{As}_2$. *EPL* **83**, 47001 (2008).
- [10] Liu, C. *et al.* K-Doping Dependence of the Fermi Surface of the Iron-Arsenic $\text{Ba}_{1-x}\text{K}_x\text{Fe}_2\text{As}_2$ Superconductor Using Angle-Resolved Photoemission Spectroscopy. *Phys. Rev. Lett.* **101**, 177005 (2008).
- [11] Castellán, J.-P. *et al.* Effect of Fermi Surface Nesting on Resonant Spin Excitations in $\text{Ba}_{1-x}\text{K}_x\text{Fe}_2\text{As}_2$. *Phys. Rev. Lett.* **107**, 177003 (2011).
- [12] Lee, C. *et al.* Incommensurate Spin Fluctuations in Hole-Overdoped Superconductor KFe_2As_2 . *Phys. Rev. Lett.* **106**, 067003 (2011).
- [13] Luo, H. *et al.* Electron doping evolution of the anisotropic spin excitations in $\text{BaFe}_{27x}\text{Ni}_x\text{As}_2$. *Phys. Rev. B* **86**, 653 (2012).
- [14] Kasahara, S. *et al.* Electronic nematicity above the structural and superconducting transition in $\text{BaFe}_2(\text{As}_{1-x}\text{P}_x)_2$. *Nature* **486**, 382–385 (2012).
- [15] Allan, M. P. *et al.* Anisotropic impurity states, quasi-particle scattering and nematic transport in underdoped $\text{Ca}(\text{Fe}_{1-x}\text{Co}_x)_2\text{As}_2$. *Nature Physics AOP* (2013).
- [16] Krüger, F., Kumar, S., Zaanen, J. & van den Brink, J. Spin-orbital frustrations and anomalous metallic state in iron-pnictide superconductors. *Phys. Rev. B* **79**, 054504 (2009).
- [17] Lv, W., Wu, J. & Phillips, P. Orbital ordering induces structural phase transition and the resistivity anomaly in iron pnictides. *Phys. Rev. B* **80**, 224506 (2009).
- [18] Chen, C.-C. *et al.* Orbital order and spontaneous orthorhombicity in iron pnictides. *Phys. Rev. B* **82**, 100504(R) (2010).
- [19] Inoue, Y., Yamakawa, Y. & Kontani, H. Impurity-induced electronic nematic state and C_2 -symmetric nanostructures in iron pnictide superconductors. *Phys. Rev. B* **85**, 224506 (2012).
- [20] Fernandes, R., Chubukov, A. V., Knolle, J., Eremin, I. & Schmalian, J. Preemptive nematic order, pseudogap, and orbital order in the iron pnictides. *Phys. Rev. B* **85**, 024534 (2012).
- [21] Chandra, P., Coleman, P. & Larkin, A. I. Ising transition in frustrated Heisenberg models. *Phys. Rev. Lett.* **64**, 88–91 (1990).
- [22] Xu, C., Müller, M. & Sachdev, S. Ising and spin orders in the iron-based superconductors. *Phys. Rev. B* **78**, 020501 (2008).
- [23] Fang, C., Yao, H., Tsai, W.-F., Hu, J. & Kivelson, S. A. Theory of electron nematic order in LaFeAsO . *Phys. Rev. B* **77**, 224509 (2008).
- [24] Kamiya, Y., Kawashima, N. & Batista, C. Dimensional crossover in the quasi-two-dimensional Ising-O(3) model. *Phys. Rev. B* **84**, 214429 (2011).
- [25] Chubukov, A. V., Efremov, D. V. & Eremin, I. Magnetism, superconductivity, and pairing symmetry in iron-based superconductors. *Phys. Rev. B* **78**, 134512 (2008).
- [26] Hassinger, E. *et al.* Pressure-induced Fermi-surface reconstruction in the iron-arsenide superconductor $\text{Ba}_{1-x}\text{K}_x\text{Fe}_2\text{As}_2$: Evidence of a phase transition inside the antiferromagnetic phase. *Phys. Rev. B* **86**, 140502 (2012).
- [27] Avci, S. *et al.* Phase diagram of $\text{Ba}_{1-x}\text{K}_x\text{Fe}_2\text{As}_2$. *Phys. Rev. B* **85**, 184507 (2012).
- [28] Avci, S. *et al.* Magnetoelastic coupling in the phase diagram of $\text{Ba}_{1-x}\text{K}_x\text{Fe}_2\text{As}_2$ as seen via neutron diffraction. *Phys. Rev. B* **83**, 172503 (2011).
- [29] Nandi, S. *et al.* Anomalous Suppression of the Orthorhombic Lattice Distortion in Superconducting $\text{Ba}(\text{Fe}_{1-x}\text{Co}_x)_2\text{As}_2$ Single Crystals. *Phys. Rev. Lett.* **104**, 057006 (2010).
- [30] Fernandes, R. M. *et al.* Unconventional pairing in the iron arsenide superconductors. *Phys. Rev. B* **81**, 140501 (2010).
- [31] Vorontsov, A. B., Vavilov, M. G. & Chubukov, A. V. Superconductivity and spin-density waves in multiband metals. *Phys. Rev. B* **81**, 174538 (2010).

SUPPLEMENTARY INFORMATION

Methods

The synthesis of homogeneous single phase $\text{Ba}_{1-x}\text{Na}_x\text{Fe}_2\text{As}_2$ polycrystalline powders was performed using conditions that are similar to $\text{Ba}_{1-x}\text{K}_x\text{Fe}_2\text{As}_2$. Further details of the synthesis can be found in Ref. [1]. Handling of all starting materials was carried out in a N_2 -filled glove box. Mixtures of Ba, Na, and FeAs were loaded in alumina tubes, sealed in niobium tubes under argon, and sealed again in quartz tubes under vacuum. The mixtures were heated at 850°C for one day and ground to homogeneous powders and then reheated for 3 days at 850°C . This last step was performed twice. Initial characterization of the the final black powders was performed by x-ray diffraction, magnetization measurements, and Inductively Coupled Plasma (ICP) elemental analysis. Powder diffraction experiments were performed on three time-of-flight neutron diffractome-

ters, HRPD ($x = 0, 0.24$) and WISH ($0.15, 0.24$) at the ISIS Pulsed Neutron Source (Rutherford Appleton Laboratory) and HIPD ($0.1, 0.2, 0.3$) at the Lujan Neutron Scattering Center (Los Alamos National Laboratory). Synchrotron x-ray diffraction measurements were performed as a function of temperature for $x = 0, 0.1, 0.15, 0.2$ at 11BM-B at the Advanced Photon Source of Argonne National Laboratory. The nuclear and magnetic structures and internal parameters were determined by the Rietveld technique using GSAS [2] and EXPGUI [3].

Theory of the Reentrant C_4 Phase

The magnetic phase in most parent compounds of the iron-based superconductors is the stripe spin-density wave order with momentum either $\mathbf{Q}_X = (0, \pi)$ or $\mathbf{Q}_Y = (\pi, 0)$ in the unfolded Brillouin zone, in which there is one iron atom per unit cell [4, 5] (see Fig. 1(b) in the main manuscript). These two wavevectors connect the hole pockets at the center of the Brillouin zone and the electron pockets at the zone boundary, along the two orthogonal iron-iron bond directions. The stripe magnetic ordering breaks both $O(3)$ spin-rotational symmetry and C_4 lattice rotational symmetry (by selecting either \mathbf{Q}_X or \mathbf{Q}_Y), and is often preceded by a “nematic” phase in which C_4 symmetry is broken, but $O(3)$ rotational symmetry remains unbroken.

In general, the geometry of iron pnictides allows more complex orders in which both Δ_X and Δ_Y are present. Previous analysis by two of us [6] have shown that near T_N , when Ginzburg-Landau theory is valid, the system definitely prefers a stripe order in which only the order parameter with \mathbf{Q}_X or \mathbf{Q}_Y is non-zero. Here we extend the previous analysis to lower T and study the magnetic order between $T = T_N$ and $T = 0$. Our results show that the phase diagram of the system is more complex than previously thought. In particular, we find that at some range of dopings, the system undergoes a first-order transition, upon lowering T , into a phase in which there is a two-component order parameter with equal magnitudes of the components with \mathbf{Q}_X and \mathbf{Q}_Y , and the four-fold lattice rotational symmetry is restored (we label this phase as a C_4 phase). The first order phase transition between the C_2 stripe and C_4 phases is consistent with the observed by neutron diffraction experiments reported in the main text.

We consider the minimal three-band model with the hole pocket Γ at the center of the Brillouin zone and two electron pockets X and Y at \mathbf{Q}_X and \mathbf{Q}_Y , respectively. For simplicity, we consider parabolic dispersions with $\xi_{\Gamma, \mathbf{k}} = \varepsilon_0 - \frac{k^2}{2m} - \mu$, $\xi_{X, \mathbf{k}+\mathbf{Q}_X} = -\varepsilon_0 + \frac{k_x^2}{2m_x} + \frac{k_y^2}{2m_y} - \mu$, and $\xi_{Y, \mathbf{k}+\mathbf{Q}_Y} = -\varepsilon_0 + \frac{k_x^2}{2m_x} + \frac{k_y^2}{2m_y} - \mu$, where m_i denotes the band masses, ε_0 is the offset energy, and μ is the chemical

potential. Near the Fermi energy and for small ellipticity, the dispersions can be approximated by $\xi_{\Gamma, \mathbf{k}} = -\xi$, $\xi_{X, \mathbf{k}+\mathbf{Q}_X} = \xi - \delta_0 + \delta_2 \cos 2\theta$, $\xi_{Y, \mathbf{k}+\mathbf{Q}_Y} = \xi - \delta_0 - \delta_2 \cos 2\theta$, with $\delta_0 = 2\mu$, $\delta_2 = \varepsilon_0 m(m_x - m_y)/(2m_x m_y)$, and $\theta = \tan^{-1} k_y/k_x$ [9].

Electrons with spin α of the band i are created by the operators $c_{i, \mathbf{k}\alpha}^\dagger$, and free-fermion part of the Hamiltonian has the form

$$\mathcal{H}_0 = \sum_{i, \mathbf{k}} \xi_{i, \mathbf{k}} c_{i, \mathbf{k}\alpha}^\dagger c_{i, \mathbf{k}\alpha} \quad (5)$$

Here the summation over repeated spin indices is assumed, and we shift the momenta of the fermions near the X and Y Fermi pockets by \mathbf{Q}_X and \mathbf{Q}_Y , respectively, i.e., write $\xi_{X, \mathbf{k}+\mathbf{Q}_X} = \xi_{X, \mathbf{k}}$, $\xi_{Y, \mathbf{k}+\mathbf{Q}_Y} = \xi_{Y, \mathbf{k}}$.

To shorten presentation, we restrict the interacting part of Hamiltonian to the interaction in the spin channel with momenta near \mathbf{Q}_X and \mathbf{Q}_Y , i.e., to

$$\mathcal{H}_{\text{int}} = -\frac{1}{2} U_{\text{spin}} \sum_{i, \mathbf{q}} \mathbf{s}_{i, \mathbf{q}} \cdot \mathbf{s}_{i, -\mathbf{q}} \quad (6)$$

where $\mathbf{s}_{i, \mathbf{q}} = \sum_{\mathbf{k}} c_{\Gamma, \mathbf{k}+\mathbf{q}\alpha}^\dagger \sigma_{\alpha\beta} \mathbf{c}_{i, \mathbf{k}\beta}$ is the electronic spin operator, and $\sigma_{\alpha\beta}$ are Pauli matrices. The coupling U_{spin} is the sum of density-density and pair-hopping interactions between hole and electron states ($U_{\text{spin}} = U_1 + U_3$ in the notation of Ref. [11]), where

$$\begin{aligned} U_1 c_{\Gamma, \alpha}^\dagger c_{\Gamma, \alpha} c_{X, \beta}^\dagger c_{X, \beta} &= -\frac{U_1}{2} c_{\Gamma, \alpha}^\dagger \sigma_{\alpha\beta} \mathbf{c}_{X, \beta} \cdot \mathbf{c}_{X, \gamma}^\dagger \sigma_{\gamma\delta} \mathbf{c}_{\Gamma, \delta} \\ &+ (\dots) \\ U_3 c_{\Gamma, \alpha}^\dagger c_{X, \alpha} c_{\Gamma, \beta}^\dagger c_{X, \beta} &= -\frac{U_3}{2} c_{\Gamma, \alpha}^\dagger \sigma_{\alpha\beta} \mathbf{c}_{X, \beta} \cdot \mathbf{c}_{\Gamma, \gamma}^\dagger \sigma_{\gamma\delta} \mathbf{c}_{X, \delta} \\ &+ (\dots) \end{aligned} \quad (7)$$

and the dots stand for the terms with $\delta_{\alpha, \beta} \delta_{\gamma, \delta}$, which only contribute to the CDW channel. The couplings U_1 and U_3 do depend on the angle along the electron pockets [7], but for our purposes this dependence may be neglected, i.e., U_{spin} can be approximated by a constant. Once U_{spin} exceeds some critical value (which gets larger when δ_0 and δ_2 increase), the static magnetic susceptibility diverges at $(0, \pi)$ and $(\pi, 0)$, and the system develops long-range magnetic order.

To understand what kind of magnetic order wins below T_N we introduce the two spin fields $\Delta_{(\mathbf{x}, \mathbf{y})} = \mathbf{U}_{\text{spin}} \sum_{\mathbf{k}} c_{\Gamma, \mathbf{k}\alpha}^\dagger \sigma_{\alpha\beta} \mathbf{c}_{(\mathbf{x}, \mathbf{y}), \mathbf{k}\beta}$. We apply Hubbard-Stratonovich transformation, integrate out fermions, obtain the action $S[\Delta_X, \Delta_Y]$ in terms of Δ_X and Δ_Y , use saddle-point approximation $\partial S / \partial \Delta_i = 0$, and solve a set of coupled saddle-point equations for Δ_X and Δ_Y . A straightforward way to perform this calculation is to introduce the 6-dimensional Nambu operator

$$\Psi_{\mathbf{k}}^\dagger = \left(c_{\Gamma, \mathbf{k}\uparrow}^\dagger \ c_{\Gamma, \mathbf{k}\downarrow}^\dagger \ c_{X, \mathbf{k}\uparrow}^\dagger \ c_{X, \mathbf{k}\downarrow}^\dagger \ c_{Y, \mathbf{k}\uparrow}^\dagger \ c_{Y, \mathbf{k}\downarrow}^\dagger \right) \quad (8)$$

Applying the Hubbard-Stratonovich transformation and evaluating the products of the Pauli matrices, we obtain the partition function in the form [8, 10]:

$$Z = \int d\Delta_i d\Psi e^{-S[\Psi, \Delta_i]} \quad (9)$$

with the action

$$S[\Psi, \Delta_i] = - \int_k \Psi_k^\dagger \mathcal{G}_k^{-1} \Psi_k + \frac{2}{U_{\text{spin}}} \int_x (\Delta_X^2 + \Delta_Y^2) \quad (10)$$

Here $\Delta_i = |\Delta_i|$, and the Green's function \mathcal{G}_k^{-1} is given by:

$$\mathcal{G}_k^{-1} = \mathcal{G}_{0,k}^{-1} - \mathcal{V} \quad (11)$$

where the free-fermion term is

$$\mathcal{G}_{0,k} = \begin{pmatrix} \hat{G}_{\Gamma,k} & 0 & 0 \\ 0 & \hat{G}_{X,k} & 0 \\ 0 & 0 & \hat{G}_{Y,k} \end{pmatrix} \quad (12)$$

and the interaction term is

$$\mathcal{V} = \begin{pmatrix} 0 & -\hat{\Delta}_X & -\hat{\Delta}_Y \\ -\hat{\Delta}_X & 0 & 0 \\ -\hat{\Delta}_Y & 0 & 0 \end{pmatrix} \quad (13)$$

Here we introduced the 2×2 matrices $\hat{G}_{i,k} = G_{i,k} \mathbb{I}$ and $\hat{\Delta}_i = \Delta_i \cdot \sigma$, where \mathbb{I} is the identity matrix. The functions $G_{i,k}^{-1} = i\nu_n - \xi_{i,k}$ are the non-interacting single-particle Green's functions for Γ , Y , and X fermions.

It is now straightforward to integrate out the fermions, since the action is quadratic in them, and obtain the effective magnetic action:

$$S_{\text{eff}}[\Delta_X, \Delta_Y] = -\text{Tr} \ln(1 - \mathcal{G}_{0,k} \mathcal{V}) + \frac{2}{u_{\text{spin}}} \int_x (\Delta_X^2 + \Delta_Y^2) \quad (14)$$

Here $\text{Tr}(\dots)$ refers to the sum over momentum, frequency and Nambu indices. In contrast to the previous studies [6, 10], we do not perform a series expansion in powers of Δ_i^2 but analyze the full non-linear saddle-point (mean-field) solutions $\frac{\delta S}{\delta \Delta_i} = 0$ for the two cases: (i) a C_2 stripe phase, in which we set $\Delta_X \neq 0$, $\Delta_Y = 0$ and (ii) a C_4 phase in which we set $\Delta_X = \Delta_Y = \Delta$. For the case (i), the mean-field equation has the form

$$1 = 2U_{\text{spin}} \Delta_X \sum_{\mathbf{k}, i\nu_n} \frac{1}{\Delta_X^2 - G_{\Gamma,k}^{-1} G_{X,k}^{-1}} \quad (15)$$

while for the case (ii) we have

$$1 = 2U_{\text{spin}} \Delta \sum_{\mathbf{k}, i\nu_n} \frac{1}{\Delta^2 - G_{\Gamma,k}^{-1} G_{X,k}^{-1} + \Delta^2 G_{X,k}^{-1} G_{Y,k}^{-1}} \quad (16)$$

In both cases the sum over Matsubara frequencies can be evaluated exactly. For stripe magnetic order, the mean-field equation becomes

$$1 = -2U_{\text{spin}} \Delta_X \sum_{\mathbf{k}} \frac{f(E_{1\mathbf{k}}) - f(E_{2\mathbf{k}})}{E_{1\mathbf{k}} - E_{2\mathbf{k}}} \quad (17)$$

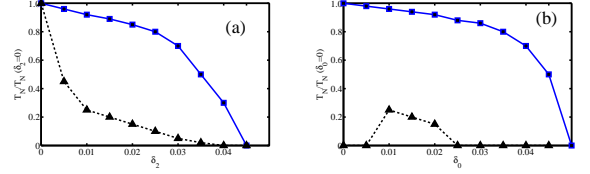


FIG. S1: (color online) Calculated magnetic phase diagram as a function of the ellipticity δ_2 at a finite mismatch between the electron and hole pockets, $\delta_0 = 0.01$ (a) and as a function of the mismatch δ_0 for the finite ellipticity $\delta_2 = 0.01$ (b). The parameter δ_0 increases with increasing doping. The squares denote the Néel temperature for the stripe phase. The triangles denote the temperature below which the C_4 phase wins over the stripe phase, although the two phases remain nearly degenerate in energy. The solid and dashed curves are guides to the eye. We used $U_{\text{sdw}} = 0.8\text{eV}$, $\epsilon_0 = 0.2\text{eV}$, and $m = 1\text{eV}$. In Fig. S1b, the energies of the C_4 and the stripe phases are very close for all T , so C_4 phase may actually win at low T in a more generic model.

where

$$E_{1,2\mathbf{k}} = \frac{1}{2} \left(\xi_{\Gamma,\mathbf{k}} + \xi_{X,\mathbf{k}+\mathbf{Q}_X} \pm \sqrt{(\xi_{\Gamma,\mathbf{k}} - \xi_{X,\mathbf{k}+\mathbf{Q}_X})^2 + 4\Delta_X^2} \right) \quad (18)$$

. For the C_4 phase, we obtain

$$1 = -2U_{\text{spin}} \Delta \sum_{\mathbf{k}} \left[\frac{(E_{11\mathbf{k}} - \xi_{X,\mathbf{k}+\mathbf{Q}_Y}) f(E_{11\mathbf{k}})}{(E_{11\mathbf{k}} - E_{22\mathbf{k}})(E_{11\mathbf{k}} - E_{33\mathbf{k}})} - \frac{(E_{22\mathbf{k}} - \xi_{X,\mathbf{k}+\mathbf{Q}_Y}) f(E_{22\mathbf{k}})}{(E_{11\mathbf{k}} - E_{22\mathbf{k}})(E_{22\mathbf{k}} - E_{33\mathbf{k}})} + \frac{(E_{33\mathbf{k}} - \xi_{X,\mathbf{k}+\mathbf{Q}_Y}) f(E_{33\mathbf{k}})}{(E_{11\mathbf{k}} - E_{33\mathbf{k}})(E_{22\mathbf{k}} - E_{33\mathbf{k}})} \right] \quad (19)$$

where the energies E_{ii} ($i = 1-3$) are the three solutions of the cubic equation $\Delta^2(\omega - \xi_{X,\mathbf{k}+\mathbf{Q}_X}) + \Delta^2(\omega - \xi_{Y,\mathbf{k}+\mathbf{Q}_Y}) - (\omega - \xi_{\Gamma,\mathbf{k}})(\omega - \xi_{X,\mathbf{k}+\mathbf{Q}_X})(\omega - \xi_{Y,\mathbf{k}+\mathbf{Q}_Y}) = 0$

We solved these equations numerically together with the equation for the chemical potential, for different values of the chemical potential mismatch δ_0 and ellipticity parameter δ_2 . Like in previous analysis [6, 8], we find that the actions for C_2 and C_4 phases are degenerate at zero ellipticity and for equal sizes of the electron and hole pockets ($\delta_0 = \delta_2 = 0$). Once ellipticity becomes non-zero, the C_2 wins near the Néel temperature. Within the Ginzburg-Landau expansion to order $\Delta_{X,Y}^4$, the lower free energy of the C_2 phase is the consequence of the fact that the ellipticity generates the term $C|\vec{\Delta}_X|^2|\vec{\Delta}_Y|^2$ with positive coefficient C , which increases the energy of the C_4 phase but does not affect C_2 phase. Going beyond Ginzburg-Landau approximation, we found that for small enough ellipticity, the solution of Eq. (19) re-emerges below some $T < T_N$ and, below this T , C_4 phase becomes a local minimum. Furthermore, in some range of Δ_2 , at even lower $T < T_{N2}$, the free energy of the C_4 phase becomes slightly smaller than that of the C_2

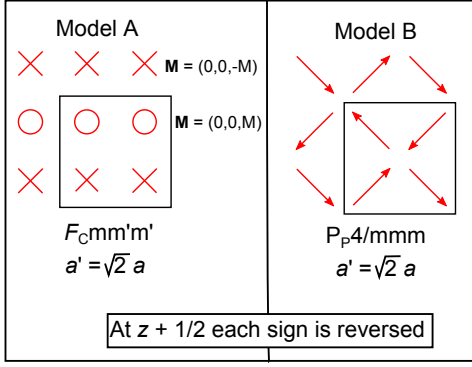


FIG. S2: The two magnetic models for the reentrant tetragonal phase that best fit the data. In Model A, the circles and crosses represent moments that are parallel and anti-parallel, respectively, to the c -axis.

phase, i.e., the system undergoes a first-order transition from C_2 to C_4 magnetic phase, and lattice C_4 symmetry gets restored.

At $\delta_0 = 0$ the region of δ_2 where C_4 phase wins is exponentially small. However, at a finite δ_0 , this region widens up. We show the results for a particular δ_0 in Fig. S1(a) and for a given ellipticity as a function of δ_0 in Fig. S1(b). A non-zero δ_0 means that the sizes of electron and hole pockets are non-equal, i.e., that there is a finite amount of doping. The implication of this result is that, at a finite doping, as the temperature is lowered, the system first orders into a stripe C_2 phase in which four-fold lattice rotational symmetry is broken (X and Y directions become non-equivalent), and then, at a lower T , it undergoes a first order transition into the C_4 phase in which four-fold lattice rotational symmetry is restored. This is consistent with our experiment.

Possible Magnetic Ordering in the C_4 Phase

High resolution neutron diffraction on HRPD (ISIS Facility) shows that the atomic structure of the C_4 phase has the same $I4/mmm$ space group as the high-temperature paramagnetic phase, but coexists with the C_2 phase with the orthorhombic $Fmmm$ space group below $T_{N_2} = 39$ K (see Fig. 3 of the manuscript). Since the ordered moments are so small (~ 0.4 to $0.8\mu_B$), the magnetic peaks are too weak to be observed on HRPD, but are measurable on the Wish diffractometer (ISIS Facility), where they are comparable in intensity to Bragg peaks due to Fe_2As and other impurity phases. This makes a completely unambiguous refinement of the magnetic structure, and even the direction of the magnetic moments, impossible. However, the symmetry imposed by the atomic structure and the constraints imposed by the data allow us to focus on the models discussed below.

Most simple magnetic models can be ruled out due to their inability to fit the large increase in intensity in the

$(101)_F$ peak that coincides with the C_4 phase (the subscript denotes that it is indexed based on the F -centered $a' = \sqrt{2}a$ cell). Only two models fit the data satisfactorily (Fig. S2). In the first (A), the magnetic moment is oriented in the c direction, with stripes in either the a or b direction (which are equivalent). In this case the magnetic space group is $Fcmm'm'$. In the second model (B), there are no stripes; instead the moments lie in the ab plane, spacegroup P_P4/mmm (P_C4/mmm with respect to the $I4/mmm$ cell). Moments adopt orientations in the $(110)_F$ directions, with the C_4 axis mandating that each moment is orthogonal to its nearest neighbor (this is the model illustrated in Fig. 1(c) in the main manuscript). In both A and B models, each layer is coupled antiferromagnetically to its neighbor, which is determined by the intensity of the magnetic $(10l)_F$ reflections. (In the AFM case $(10l) = 0$ for $l = 2n$ and in the FM case $(10l) = 0$ for $l = 2n + 1$. We observe the former.)

The fits to the two co-existing phases observed below 39 K, i.e., the C_4 phase (models A or B) and the C_2 stripe phase, are compared in Fig. S3. Model A produces a slightly better overall fit than model B. However, the weak signal-to-noise ratio and the overlap with peaks from the coexisting C_2 magnetic phase as well as weak impurity phases preclude an unambiguous solution. The magnetic moments reported in the manuscript (see Fig. 4 in the main manuscript) for the C_4 and C_2 phases are based on a free refinement of the moments for the C_4 model A and the standard C_2 model.

Relationship of Magnetic Ordering to the Theoretical Electronic Model

The atomic structure of the C_4 phase is tetragonal, with no evidence of orthorhombic strain even in the high resolution measurements on HRPD. This implies by symmetry that $J_a = J_b$, which is consistent with Model B, whose magnetic space group is also tetragonal. However, the magnetic structure of Model A is still apparently orthorhombic even though the moments are along the c -axis. This cannot be reconciled with an orbital order

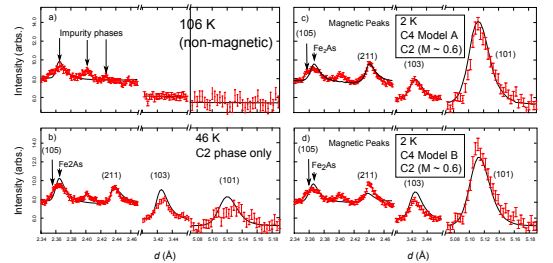


FIG. S3: Fits to the principal magnetic peaks at various temperatures: a) 106 K (tetragonal non-magnetic), b) 46 K (orthorhombic phase only), c) 2 K (tetragonal model A + orthorhombic), and d) 2 K (tetragonal model B + orthorhombic). All plots are on same scale, error bars are d -dependent in neutron time-of-flight measurements.

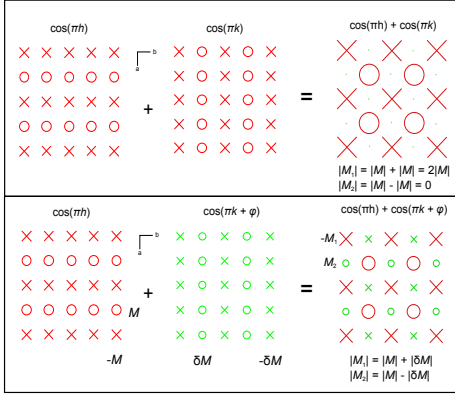


FIG. S4: Upper panel: A combination of the two equivalent arms in model A gives a checkerboard with half moments equal to zero. Lower panel: Adding the arms out of phase yields incomplete cancellation of moments in the SDW model.

model, in which the stripes are a result of $J_a \neq J_b$, but it is also not consistent with the itinerant model, in which the a and b axes are equivalent. However, tetragonal symmetry can be restored if we assume that, instead of separate domains of a and b -axis stripes, the magnetic structure involves a simultaneous modulation in both directions, *i.e.*, a double- k structure.

Writing the two forms as a spin-density waves with modulations $\cos(\pi h)$ and $\cos(\pi k)$ shows that adding the waves interfere such that half of the moments double and the others sum to zero (Fig. S4: upper panel). The nodes on every other Fe atom in a checkerboard fashion remove striping and recover tetragonal symmetry. In an itinerant magnetic model, a node implies that there is actually zero moment centered on the nodal atom (unlike localized moment systems where nodes in a magnetic model imply a fluctuating spin and therefore contribute a significant entropy to the system). This is physically allowed but an alternative choice without nodes is to change the phasing between waves, *e.g.*, $\cos(\pi k) + \cos(\pi k + \phi)$, which scales the amplitude of one direction because $\cos(\pi k + \phi) = \pm \delta$ where $0 \leq \delta \leq 1$. This gives a situation where $|M_1| = |M| + \delta$ and $|M_2| = |M| - \delta$. This gives a checkerboard of alternating large and small moments (Fig. S4: lower panel). This can be modeled in tetragonal space groups without a proper C_4 axis, such as $P4_2$ and $P\bar{4}$ which allow for two inequivalent coplanar Fe atoms. We modeled this arrangement (model A2) in the spacegroup $P\bar{4}'2_1c'$ (#114). This maintains the striping, but there is an intractable difference between models A and A2. The $\bar{4}$ axis preserve tetragonal symmetry by requiring

that the striping alternates directions between layers, so that there is no preferred direction (left panel, Fig. S5). Thus, the only situation that is fully AFM coupled between layers is when $M_2 = 0$. This makes unobserved reflections ($102n$) non-zero. However, situations where $M_1^2 \gg M_2^2$ (right panel, Fig. S5) predict intensities for these peaks that are on the same scale as the noise. Otherwise the two models are identical. In short, Model A is a more elegant solution to the magnetic data than A2. However, a final determination of the magnetic structure will have to wait for single crystal measurements.

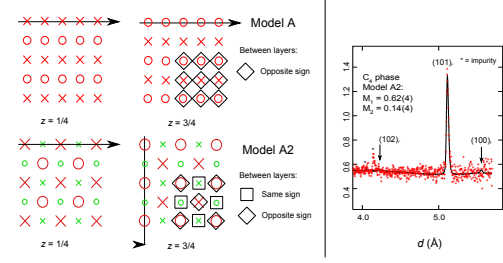


FIG. S5: Left panel: Comparison of the differences between layers in the magnetic models A and A2 described in the text. Right panel: An example of a refinement of Model A2.

- [1] Avci, S. *et al.* Phase diagram of $\text{Ba}_{1-x}\text{K}_x\text{Fe}_2\text{As}_2$. *Phys. Rev. B* **85**, 184507 (2012).
- [2] Larson, A. C. & Von Dreele, R. B. General Structure Analysis System (GSAS). Tech. Rep. LAUR 86-748, Los Alamos National Laboratory (2000).
- [3] Toby, B. H. EXPGUI, a graphical user interface for GSAS. *J. Appl. Cryst.* **34**, 210–213 (2001).
- [4] T. Yildirim, *Phys. Rev. Lett.* **101**, 057010 (2008).
- [5] F. Ma, Z.-Y. Lu, and T. Xiang, *Phys. Rev. B* **78**, 224517 (2008).
- [6] I. Eremin and A. V. Chubukov, *Phys. Rev. B* **81**, 024511 (2010).
- [7] Ying Ran, Fa Wang, Hui Zhai, Ashvin Vishwanath, and Dung-Hai Lee *Phys. Rev. B* **79**, 014505 (2009).
- [8] R. M. Fernandes and J. Schmalian *Phys. Rev. B* **82**, 014521 (2010).
- [9] A B Vorontsov, M G Vavilov, and Andrey V Chubukov, *Phys. Rev. B* **81**, 174538 (2010).
- [10] R.M. Fernandes, A.V. Chubukov, J. Knolle, I. Eremin, and J. Schmalian, *Phys. Rev. B* **85**, 024534 (2012)
- [11] A. V. Chubukov, D. V. Efremov, and I. Eremin, *Phys. Rev. B* **78**, 134512 (2008)